Research Square

Preprints are preliminary reports that have not undergone peer review.
They should not be considered conclusive, used to inform clinical practice,
or referenced by the media as validated information.

# Creep-Free Ionic Elastomer for Non-drifting Ear-EEG Signal Acquisition

**Qin Yue**

qinyue@uestc.edu.cn

University of Electronic Science and Technology of China https://orcid.org/0000-0002-4687-1747

**Ruiming Liu**

University of Electronic Science and Technology of China

**Xueyang Ge**

Northwestern Polytechnical University

**Xiaojun Zhang**

University of Electronic Science and Technology of China

**Zijun Xu**

Xi'an Jiaotong University

**Yanning Zhang**

University of Electronic Science and Technology of China https://orcid.org/0000-0002-3839-2965

**Xiaosen Pan**

Xi'an Jiaotong University https://orcid.org/0000-0002-2760-4598

**Zhenwen Li**

University of Electronic Science and Technology of China

**Lihong Yang**

The Hong Kong Polytechnic University

**Article**

**Keywords:**

**Posted Date:** December 16th, 2025

**DOI:** https://doi.org/10.21203/rs.3.rs-7776781/v1

**License:** This work is licensed under a Creative Commons Attribution 4.0 International License.
Read Full License

**Additional Declarations:** There is **NO** Competing Interest.

**Version of Record:** A version of this preprint was published at Nature Communications on September 15th, 2026. See the published version at https://doi.org/10.1038/s41467-026-77777-6.

# Abstract

Monitoring and identification of ear electroencephalogram (Ear-EEG) signals offer a promising non-invasive approach for tracking mental states. Compared to rigid metal electrode, polymer electrodes possess flexibility, good biocompatibility, superior skin adhesion, and wearing comfort, however, their accuracy is often compromised by signal drift due to polymer creep under sustained strain. To address this, we introduce a molecular strategy that suppresses creep by compensating entropy loss through a designed intramolecular dihedral structure. The copolymer integrates two distinct crosslinks: flexible segments stabilized by electrostatic self-coordination, and a minority of rigid segments formed by covalent main-chain bridges. In-situ scattering and theoretical simulations confirm that the covalently bridged TAO segments adopt a rigid dihedral configuration, effectively restraining chain slippage and eradicating viscoelasticity. Concurrently, dynamic disulfide exchange further enhances network stability under deformation. This design yields the novel creep-free polyelectrolyte ionic elastomer, denoted as Poly(TA-*co*-TAT)-TAO, which demonstrates outstanding stretchability (> 200%) and elasticity (hysteresis < 7.5%, recovery > 99% at 160% strain). Leveraging its persistent creep resistance (< 0.4% over 12 hours), the resulting wearable EEG device enables reliable, long-term mental status monitoring in real-world settings.


# Introduction

Reliable and long-term monitoring of neurophysiological states is significant and necessary in daily monitoring of psychiatric condition.[1–3] Electroencephalogram (EEG) signals provide among the most direct physiological reflections of mental status. However, conventional EEG systems relying on rigid electrodes are limited by mechanical mismatch[4], invasiveness[5], and poor portability[6], which hinder comfortable and prolonged recording. Ear-EEG has emerged as a promising non-invasive alternative, offering excellent wearability and compatibility for continuous monitoring[7]. However, existing polymer conductors are unsuitable for Ear-EEG monitoring due to their intrinsic signal drift, which compromises signal accuracy[8].

Signal drift in polymer electrodes primarily arises from ion leakage within the polymer network or material creep. While conductive ionic gels are widely employed as polymer electrodes, their potential ion leakage toxicity limits their suitability for skin-contact applications. Current polyelectrolyte elastomers mitigate leakage by immobilizing cations/anions on the polymer backbone. However, this constraint on ionic mobility compromises the network's capacity for energy dissipation and stress release, increasing susceptibility to fracture under prolonged stress[9]. Additionally, creep in polyelectrolyte elastomers, driven by polymer chain slippage[10] or molecular rearrangement[11], modifies the ion–electron interface contact area, inducing signal drift. Addressing this requires that entropic elasticity substantially outweighs viscoelasticity to achieve creep resistance[12]. Although increasing covalent crosslinking density enhances entropic elasticity, it does not significantly suppress viscoelasticity and it also cause the raised Young's modulus of the elastomer[13,14], which leads to poor

flexibility. Thus, the central challenge lies in designing creep-free polyelectrolyte elastomers that eliminate viscoelasticity while maintaining low modulus and high ionic conductivity stability, essential for long-term reliable EEG signal acquisition.

In this study, a creep-free ionic elastomer with low Young's modulus is developed for the first time through rational molecular design for stable electroencephalography (EEG) signal acquisition. The zwitterionic elastomer is synthesized by immobilizing cations onto carboxyl groups located on the side chains of thioctic acid, while specific crosslinking molecules are introduced to bridge polymer chains and suppress long-range segmental motion. In-situ scattering analyses and theoretical simulations reveal that the covalently bridged TAO segments form a rigid dihedral architecture between main chains, effectively inhibiting chain slippage and eliminating viscoelasticity. Concurrently, dynamic disulfide bond exchange promotes network stabilization under sustained deformation, contributing to the low modulus. The resulting elastomer demonstrates near-zero creep under a constant stress of 50 kPa, with an initial drift rate as low as 0.04–0.1% $min^{-1}$, while maintaining low stiffness. The derived polymer electrode exhibits negligible signal drift over 12 hours at 45% strain. Its combination of low modulus and high intrinsic ionic conductivity ensures stable ion-electron coupling at the skin–electrode interface, enabling comfortable, sensor-free wear. This creep-free soft electrode facilitates precise, long-term monitoring of EEG signals with high fidelity.

## Design concept of the creep-free polyelectrolyte elastomer

Conventional ionic elastomers often exhibit creep under sustained stress due to polymer chain slippage or molecular rearrangement, resulting in signal drift. To overcome this limitation, a creep-free, self-coordinating zwitterionic elastomer was designed by immobilizing the cations onto carboxyl groups located on the side chains of thioctic acid and introducing specific crosslinking molecules to bridge polymer chains and form unique rigid dihedral architecture(Fig. 1a). This random copolymer network contains two types of crosslinks: a majority of branched segments that self-coordinate via electrostatic interactions (flexible segments), and a minority of covalently crosslinked main-chain segments (rigid segments) (Supplementary Fig. 1). The ions are fixed to the polymer backbone without solvents, preventing leakage. Electrostatic interactions enable energy dissipation and elastic recovery. Under external stress, the self-coordinating branched chains balance the elastic forces from entropy-driven chain deformation: 1) Under compression, the anionic and cationic ends approach each other, generating repulsion between branched chains; 2) Under stretching, the electrostatic attraction between the branched chains increases. Modeling the polymer network as a standard linear solid—an elastic spring (stiffness $k$) in parallel with a Maxwell arm—the electrostatic interactions act as a damper (viscosity $\eta$), accounting for its viscoelastic behavior. The incorporated rigid segments increase crosslinking density, enhancing entropy elasticity (increasing $k$) while restricting long-range ion mobility. This restriction exponentially raises the effective viscosity ($\eta > 10^9$ Pa·s), approximating the damper as a rigid link. Consequently, when the applied stress is predominantly supported by the elastic springs $k$ and $k'$, the network becomes nearly creep-free[12].

# Structure characterizations

The creep-free polyelectrolyte elastomer is composed of thioctic acid (TA), ionized thioctic acid ester (TAT, $C_{17}H_{25}O_6S_4N_3F_6$), and thioctic acid–tetraethylene glycol ester (TAO, $C_{24}H_{42}O_7S_4$) (Fig. 1b). Unless specified otherwise, the elastomer without TAO is denoted as Poly(TA-*co*-TAT), and the formulation containing TAO is referred to as Poly(TA-*co*-TAT)-TAO. Successful monomer synthesis was confirmed by Nuclear magnetic resonance (NMR, $^{1}H$, $^{13}C$, $^{19}F$), high-resolution mass spectrometry, FTIR, and Raman spectroscopy (Supplementary Figs. 2–8). The resulting elastomer was amorphous and stable without depolymerization (Supplementary Fig. 9). Raman spectra showed that the disulfide ring-opening polymerization split the characteristic peak at 510 $cm^{-1}$ in monomeric TA into two bands at 508 and 524 $cm^{-1}$ in both Poly(TA-*co*-TAT) and Poly(TA-*co*-TAT)-TAO, confirming successful polymerization (Supplementary Fig. 10a). In Poly(TA-*co*-TAT)-TAO, the C = O stretching vibration shifted to a higher frequency (from 1689 to 1731 $cm^{-1}$), indicating stronger ester bonds due to intermolecular ionic interactions (Fig. 1c and Supplementary Fig. 10b)[15,16]. Gel permeation chromatography revealed a number-average molecular weight ($M_n$) of ~ $2.47 \times 10^4$ g·$mol^{-1}$ for Poly(TA-*co*-TAT)-TAO, corresponding to approximately 30 repeat units per chain (Supplementary Fig. 11). Molecular dynamics simulations confirmed the presence of self-coordinating zwitterionic interactions through interaction energy calculations (Fig. 1d). These electrostatic interactions stabilize the polydisulfide network, raising its melting temperature to 105°C and maintaining thermal stability even up to 230°C (Supplementary Figs. 12–13). Atomic force microscopy showed that Poly(TA-*co*-TAT)-TAO has a smoother surface and more uniform elemental distribution than poly(thioctic acid) (PolyTA) (Fig. 1$\mathbf{e_i}$, Supplementary Figs. 14–15), likely due to introduced electrostatic interactions. A phase diagram further revealed the formation of an irregularly distributed hard phase within Poly(TA-*co*-TAT)-TAO (Fig. 1$\mathbf{e_{ii}}$, Supplementary Figs. 14$a_{ii}$, 14$b_{ii}$). The reduced phase lag indicated lower energy dissipation, suggesting that hard segments restrict the dissociation of electrostatic interactions. Wide-angle X-ray scattering results showed that the hard segments increase the average chain spacing in the polydisulfide network, expanding the reversible migration space for coordinating ions (Fig. 1f).

# Creep-free behavior and mechanism analysis

The effect of TAO-induced hard segments on the creep resistance of elastomers was evaluated through comparing the mechanical and rheological properties of Poly(TA-*co*-TAT)-TAO and Poly(TA-*co*-TAT). As temperature increased, the two materials showed significantly different extent of stress relaxation. Under identical initial strain, Poly(TA-*co*-TAT) exhibited rapid and nearly complete stress relaxation starting at 30°C (Fig. 2$\mathbf{a_i}$). In contrast, Poly(TA-*co*-TAT)-TAO maintained the stress over prolonged duration (> 15 min) from 30 to 60°C, with detectable relaxation occurring only at 70°C (Fig. 2$\mathbf{a_{ii}}$). It implied the hard segments in Poly(TA-*co*-TAT)-TAO enhance its structural stability by restricting electrostatic dynamics. The creep and recovery tests under varying loads (Fig. 2$b_i$ and 2$b_{ii}$) showed that Poly(TA-*co*-TAT) exhibits continuous increases in strain over time, indicating pronounced creep (Fig. 2$\mathbf{b_i}$).

In contrast, Poly(TA-*co*-TAT)-TAO demonstrated effective resistance to deformation (Fig. 2**b$_{ii}$**). The persistent creep in Poly(TA-*co*-TAT) suggests that electrostatic bonds break readily under load, resulting in irreversible network deformation. Creep and recovery curves under 9 kPa are provided in Supplementary Fig. 16. Poly(TA-*co*-TAT) exhibited substantially greater creep strain than Poly(TA-*co*-TAT)-TAO, attributing to chain slippage and molecular rearrangement (Supplementary Figs. 16a–b). Moreover, Poly(TA-*co*-TAT)-TAO had negligible residual strain and high recovery ratio across all loading conditions (Fig. 2**b$_{i}$**, **2b$_{ii}$**). Calculation of equivalent damper viscosity from residual strain showed that the average viscosity of Poly(TA-*co*-TAT)-TAO was three orders of magnitude higher than that of Poly(TA-*co*-TAT) (Supplementary Fig. 17). Additional creep tests at elevated temperatures confirmed that Poly(TA-*co*-TAT)-TAO possess a more stable network, with significantly improved creep resistance (Supplementary Figs. 18a–d).

To further investigate the dynamic mechanical behavior of Poly(TA-*co*-TAT)-TAO and Poly(TA-*co*-TAT) across different time scales, master curves were constructed using the time-temperature superposition (TTS) principle at 30°C. As shown in Fig. 2**c$_{i}$**, the storage modulus of Poly(TA-*co*-TAT) decreased rapidly at low frequencies, reflecting substantial relaxation of its electrostatic crosslinking network. In contrast, Poly(TA-*co*-TAT)-TAO maintained a high elastic modulus (> $10^5$ Pa) even at 90°C, demonstrating significantly improved network stability (Fig. 2**c$_{ii}$**). The horizontal shift factors ($a_T$) derived from the master curves are presented in Supplementary Fig. 19. Both materials exhibited strong temperature dependence above 40°C, obeying the Arrhenius law. Fitting these values yielded apparent activation energies ($E_a$) of 78.4 kJ·mol$^{-1}$ for Poly(TA-*co*-TAT)-TAO and 35.7 kJ·mol$^{-1}$ for Poly(TA-*co*-TAT). $E_a$ reflects the energy required for dissociation of noncovalent crosslinks[17], the higher value for Poly(TA-*co*-TAT)-TAO suggests that electrostatic interactions constrained by hard segments form more stable crosslinks, thereby enhancing network integrity. Further insight into the enhanced stability was gained through variable-temperature Fourier transform infrared spectroscopy (VT-FTIR). As temperature increased, the C = O stretching vibration in Poly(TA-*co*-TAT) shifted from 1731 cm$^{-1}$ to 1728 cm$^{-1}$, indicating weakening of electrostatic interactions (Fig. 2**d$_{i}$**). In contrast, no shift was observed for Poly(TA-*co*-TAT)-TAO, confirming its superior thermal and structural stability (Fig. 2**d$_{ii}$**). These results underscore the beneficial role of TAO in stabilizing the elastomeric network against thermal and mechanical relaxation.

In situ WAXS and SAXS analyses were performed to study the structural evolution of Poly(TA-*co*-TAT)-TAO and Poly(TA-*co*-TAT) under stretching (Fig. 2e and Supplementary Figs. 20–24). Prior to deformation, the isotropic scattering rings in the 2D SAXS/WAXS patterns suggested that Poly(TA-*co*-TAT)-TAO is amorphous, isotropic, and phase-separated (Fig. 2e, Supplementary Figs. 21a and 22a-b). Upon stretching, the WAXS patterns remained isotropic, as confirmed by azimuthal integration (Supplementary Figs. 23a–b). Furthermore, the material exhibited enhanced phase separation under strain. When the strain was released, the 1D WAXS profile nearly returned to its initial state, indicating full structural recovery (Fig. 2e and Supplementary Fig. 20). In contrast, Poly(TA-*co*-TAT) showed residual strain after returning to 0% strain (Supplementary Figs. 21a–e and 23c–d). No significant orientation was observed in the SAXS patterns of Poly(TA-*co*-TAT)-TAO during stretching, suggesting that the hard

domains remained largely unaligned, with a maximum displacement of only 0.2 nm (Fig. 2f and 2g). Similarly, Poly(TA-*co*-TAT) also exhibited no orientational change in its scattering rings; however, its phase-separated structure underwent a long-range shift of 1.6 nm under strain (Supplementary Figs. 24a–b). These findings confirm that the TAO-induced hard phase imposes a strong confinement effect on the polymer network, enhancing its stability and recovery behavior.

To elucidate the role of TAO during deformation, molecular dynamics (MD) simulations were conducted (Supplementary Fig. 25). The molecular structures and bond lengths of the monomers are provided in Supplementary Figs. 26a–c and Supplementary Table 1. Models of Poly(TA-*co*-TAT)-TAO and Poly(TA-*co*-TAT) were constructed using a dynamic cross-linking approach (Fig. 2h and Supplementary Note 1). Uniaxial stretching simulations were performed to analyze the deformation behavior of both systems (Supplementary Videos 1–2). The molecular chain mobility in Poly(TA-*co*-TAT)-TAO was reduced compared to Poly(TA-*co*-TAT), confirming that trace TAO restricts network dynamics (Supplementary Figs. 27a–b). Under strain, TAO units maintained stable relative positions within the surrounding polymer chains without fracture (Fig. 2i and Supplementary Video 2). Stress–strain curves obtained at a constant tensile rate ($10^9$ $s^{-1}$, a typical value for such simulations[18–20]) showed that Poly(TA-*co*-TAT)-TAO sustained higher stress at the same strain than Poly(TA-*co*-TAT), consistent with experimental trends (Supplementary Fig. 28a). Moreover, Poly(TA-*co*-TAT)-TAO exhibited a lower Poisson's ratio (0.417) than Poly(TA-*co*-TAT) (0.435), indicating weaker molecular relaxation (Supplementary Figs. 28b–c). Creep behavior under constant stress below the tensile strength revealed that Poly(TA-*co*-TAT) underwent greater strain than Poly(TA-*co*-TAT)-TAO under the same load (Supplementary Figs. 29a–b). The strain plateau observed in Poly(TA-*co*-TAT)-TAO suggests enhanced creep resistance. Analysis of potential energy components during tensile testing under 20 MPa stress showed that bond, angle, and improper energies remained stable and comparable in both systems. In contrast, van der Waals energy initially increased and then decreased as atomic positions adjusted relative to the potential well (Supplementary Figs. 30a–b). Notably, the electrostatic energy of Poly(TA-*co*-TAT) was higher initially but decreased during stretching, whereas Poly(TA-*co*-TAT)-TAO exhibited minimal fluctuation in electrostatic energy[21]. This difference arises because TAO introduces rigid dihedral motifs: the dihedral coefficients of the TAO ester backbone ($K_{\phi 3}$ and $K_{\phi 4}$) exceed those of the carbon–sulfur backbone ($K_{\phi 1}$ and $K_{\phi 2}$) (Fig. 2$\mathbf{j_i}$ and $\mathbf{j_{ii}}$). Higher K values correspond to greater dihedral energy, increasing overall stiffness and resistance to stretching. Consequently, Poly(TA-*co*-TAT)-TAO exhibited higher dihedral energy (Fig. 2k and Supplementary Figs. 31a–b), which restricted chain mobility, reduced deformation under stress, and contributed to its low creep.

Electron paramagnetic resonance (EPR) spectroscopy detected sulfur radicals generated within the network during stretching (Fig. 2l), confirming the occurrence of disulfide bond exchange. Under continuous stress, mechanical energy was converted into molecular potential energy and distributed across chemical bonds. Once the stored energy in a dihedral exceeded its capacity, the surplus prompted disulfide bonds to rupture and undergo local exchange, thereby maintaining the most stable network configuration under persistent load. Molecular dynamics simulations and experiments verified

that the high elasticity and creep resistance of Poly(TA-*co*-TAT)-TAO arise from the synergistic effect of dihedral restriction and dynamic disulfide bond exchange. Compared with Poly(TA-*co*-TAT), Poly(TA-*co*-TAT)-TAO exhibits higher dihedral energy upon stretching, enabling greater energy storage under stress. During stretching, external work reduces the entropy of the polymer network and alters the potential energy of the molecular chains. Upon release of stress, the network recoils driven by entropic recovery, while the extra stored dihedral energy compensates for the energy consumed in electrostatic dissociation and disulfide exchange during stretching, ultimately leading to nearly complete (≈ 100%) network rebound.

## Mechanical Properties

The mechanical properties of the elastomers with different compositions were analyzed through long-term creep-resistance tests. Poly(TAO-*co*-TAT) showed pronounced creep and fractured rapidly (< 0.5 h) (Supplementary Fig. 32a), as the absence of energy-dissipating moieties led to stress accumulation under continuous load. Poly(TA-*co*-TAT), which lacks constraints on polymer chains, also exhibited considerable creep (21.08% after 12 h) (Supplementary Fig. 32b). Variations in TAO content resulted in distinct levels of creep resistance and conductivity (Supplementary Figs. 33a–d and 34). At low TAO content, the less mobile TAO segments helped extend and stabilize molecular chains, offering stable pathways for ion transport. However, increasing TAO content led to densely interwoven chains that hindered ion mobility, reducing ion migration capability (Supplementary Figs. 35a–l). With rising TAO content, the elastomers showed higher Young's modulus and lower elongation at break (Supplementary Figs. 36a–b). At 1.0 mol% TAO, the elastomer demonstrated a creep strain of only 0.38% after 12 h and a conductivity of $1.32 \times 10^{-6}$ S/cm (Supplementary Fig. 34).

The polyelectrolyte elastomer Poly(TA-*co*-TAT)-TAO exhibited excellent creep resistance, maintaining both mechanical and electrical properties (e.g., tensile strain and resistance) under a 30 kPa load for 24 h (Fig. 3a). This stability was further confirmed under dynamic loading: the peak strain showed negligible change over 10,000 cycles under a triangular-wave stress of 30 kPa at 1 Hz (Fig. 3b). Uniaxial tensile tests compared the optimized elastomers Poly(TAO-*co*-TAT), Poly(TA-*co*-TAT), and Poly(TA-*co*-TAT)-TAO, denoted as TAT-i, TAT-ii, and TAT-iii, respectively (Fig. 3c). Among them, TAT-iii demonstrated the largest fracture strain (203.1%), highest tensile strength (181.4 kPa, Fig. 3d), highest toughness (22.7 $kJ \cdot m^{-3}$, Fig. 3e), and highest compressive strength (229.6 kPa, Fig. 3f). For brevity, the optimized Poly(TA-*co*-TAT)-TAO is hereafter referred to as TAT unless otherwise stated.

Cyclic stretching tests of TAT were conducted under various tensile strains (Fig. 3$\mathbf{g_i}$–$\mathbf{g_{ii}}$), with the resulting curves presented in two separate graphs for clarity. Figure 3h summarizes the corresponding strain recovery and hysteresis ratio. To quantitatively assess the material's resilience, the recovery efficiency ($\eta_{recovery}$) is defined as follows:

$$\eta_{recovery} = \left(1 - \frac{\varepsilon_{residual}}{\varepsilon_{max}}\right) \times 100\%$$

where $\varepsilon_{residual}$ is the residual strain upon stress returning to zero. At strains below 160%, TAT demonstrated excellent resilience ($\eta_{recovery}$ ≥ 99%) and minimal hysteresis (< 7.5%), indicating low energy dissipation in overcoming chain friction and disentanglement during short-range deformation. The hysteresis of TAT was further examined under continuous cyclic loading to 30% strain. The nearly overlapping stress-strain curves of the 1st and 1,000th cycles, with an average hysteresis of < 3.8% over 1,000 cycles (Supplementary Fig. 37 and Video 3), confirm its outstanding durability.

## Electrical Properties

Polyelectrolyte electrodes for long-term signal acquisition should possess stable conductivity without signal drift. This was quantitatively assessed under static pressure using the drift ratio and drift rate (Fig. 4a). TAT-based electrodes demonstrated significantly lower drift in both metrics compared to other polymer materials. The drift ratios of eleven sensors under 50 kPa for 10 minutes are shown in Fig. 4b. The TAT electrode had an average drift ratio of ~ 0.36%, two orders of magnitude lower than others. Its drift rate was also one to three orders of magnitude smaller at the same pressure (Fig. 4c). The TAT electrode also showed excellent signal stability under prolonged static pressure and cyclic square-wave loading. Under a static load of ~ 50 kPa, the signal drift was negligible (~ 0.27%) over 12 hours and recovered rapidly upon load release (Fig. 4d). Under a 30 kPa square-wave load (10 s per wave), the electrode produced a stable square-wave signal for over 1,000 cycles (Fig. 4e). Impedance tests confirmed stable ion migration capability throughout this cyclic compression (Fig. 4f), which was also maintained in high-humidity environments (Supplementary Fig. 38). In contrast, an ionic gel electrode with identical cation/anion types showed pronounced drift, with a 26.91% resistance increase within 10 minutes under 50 kPa (Fig. 4g). Its output signal also increased significantly during dynamic compression cycles (Fig. 4h), and impedance tests revealed rising resistance to ion migration, confirming the origin of the electrical drift (Fig. 4i).

## TAT electrode for electroencephalogram monitoring

Polymer electrodes based on non-drifting ionic elastomers are crucial for reliable electroencephalographic (EEG) signal acquisition. We evaluated TAT electrodes placed in the ear canal under various signal conditions. The inherent elasticity of TAT enables it to conform closely to the ear canal upon insertion, forming stable skin contact. The electrode–ear impedance was continuously monitored at 10 Hz (EEG alpha band, Fig. **5a**) and via electrochemical impedance spectroscopy (5 Hz–1 kHz, Fig. **5b** and Supplementary Note 2). Owing to the adaptive contact of the TAT electrode, the interface impedance stabilized within 60 seconds, effectively capturing electrical activity from the skin. The average electrode–ear impedance at 50 Hz was 39 kΩ with a contact area of 4.2 $cm^2$, comparable to

that of a commercial gel electrode (55 kΩ at 50 Hz, 6 $cm^2$ area) but with a smaller footprint. Alpha modulation—a spontaneous EEG pattern between 8–12 Hz related to visual attention or relaxation—was clearly observed. Fig. **5c** shows the synchronous appearance of alpha-band signals when the participant closed their eyes over two 10-s intervals. The grand average alpha-band power spectral density (PSD) across 10 participants (Fig. **5d**) confirmed a significant power increase in the alpha band upon eye closure. We also recorded the auditory steady-state response (ASSR), an evoked oscillation from the auditory cortex in response to amplitude-modulated acoustic stimuli (Fig. **5e**). Grand average ASSR PSDs across four participants (Fig. **5f–h**) exhibited clear peaks at the stimulus frequencies (30, 45, and 60 Hz). Although the signal-to-noise ratios were lower than those from head-mounted patch electrodes, the ear-EEG signals collected with TAT electrodes were consistent with conventional recordings, confirming their reliability (Fig. **5i**). Additionally, the TAT electrode captured electrooculography (EOG) artifacts from eye movements—often considered noise in EEG but useful in certain brain–computer interface applications[22]. With a reference electrode in the same ear, the TAT sensor clearly resolved EOG-shaped artifacts (Fig. **5j**), facilitating signal extraction or artifact removal[23,24]. For long-term monitoring, signal stability is essential. Unlike commercial gels that often drift, the TAT electrode maintained high stability and accuracy in ear-EEG applications (Fig. **5k**). Even under varying ambient temperatures, the signals remained clearly recognizable, demonstrating practical reliability (Fig. **5l**).

**Emotion detection and automatic intervention based on ear-EEG**

Non-drift polymer electrodes show promise for emotional monitoring in patients with bipolar disorder, enabling accurate emotion identification and proactive intervention (Fig. **6a**). The biocompatibility of the Poly(TA-*co*-TAT)-TAO electrode was evaluated by incubating human keratinocytes (HaCaT) on its surface for 24 hours. Fluorescence staining showed good cell adhesion, and a Cell Counting Kit-8 assay confirmed 100% cell viability, comparable to the control group (Supplementary Figs. 39a–b). We integrated TAT electrodes with a processor into a wireless wearable ear-EEG device (Fig. **6b**), which includes in-ear shaped TAT electrodes (Fig. **6c** and Supplementary Fig. 40), silver-plated conductive posts, an EEG acquisition circuit, and a Zigbee transmission module (Supplementary Fig. 41). The TAT electrode adapted well to different ear canal shapes in both left and right ears (Supplementary Fig. 42). The device collects EEG data in real time and transmits it to a computing terminal for signal processing, which extracts frequency-band features such as alpha, beta, and gamma waves (Fig. **6d**). Given the alternating manic and depressive episodes in bipolar disorder, precise frequency-band separation is essential for emotion recognition. We validated the device's accuracy in extracting alpha and theta waves during meditation, where the system successfully estimated meditation depth in real time (Fig. **6e**). Furthermore, we collected ear-EEG data from five participants (aged 22–26) under emotion induction[25], annotating signals with seven emotional categories (happiness, sadness, fear, disgust, surprise, anger, and calmness) and timestamps (Fig. **6f**). A deep neural network (DNN) combining convolutional and recurrent layers was designed to classify emotions from preprocessed EEG segments. The model output probability distributions over the seven emotions, achieving strong classification

results (Fig. **6g–h**). The trained model was embedded into the terminal for real-time emotional state feedback.

For patients with bipolar disorder, timely music intervention can help alleviate symptoms[1,2]. By integrating the emotion classifier with a music playback system, we enabled real-time emotion recognition and autonomous intervention (Supplementary Fig. 43). The wearable device acquires EEG signals, identifies emotional states, and triggers personalized music feedback in response to negative emotions like anger or depression (Supplementary Fig. 44). During prolonged emotion tests using picture induction (Fig. **6i–j**), the device accurately detected emotions such as happiness, sadness, and surprise. When negative emotions persisted, music intervention was activated promptly, helping restore emotional baseline levels (Supplementary Video 4).

# Discussion

Polymer electrodes offer distinct advantages over traditional rigid electrodes, including superior flexibility[26], excellent biocompatibility[27], close skin adhesion[28], and enhanced wearing comfort[29], making them particularly suitable for skin-contact electrodes and devices. However, their signal transmission stability and accuracy are often compromised by signal drift resulting from polymer creep under prolonged high strain. Given that creep in polymers is frequently attributable to viscoelastic behavior, we propose a strategy to compensate for entropy loss through dihedral constraints energy. The designed copolymer network incorporates two types of crosslinks: a majority of branched segments that self-coordinate via electrostatic interactions (flexible segments), and a minority of covalently crosslinked main-chain segments (rigid segments). In-situ scattering characterization combined with theoretical simulations confirms that the covalently bridged TAO segments between main chains form a unique rigid dihedral structure, which effectively suppresses chain slippage and eliminates viscoelasticity. Meanwhile, dynamic disulfide bond exchange further stabilizes the network under sustained deformation.

As a result, a creep-free polyelectrolyte ionic elastomer is synthesized for the first time, enabling signal transmission without drift and stable, accurate acquisition of electroencephalographic (EEG) signals. The resulting dynamic polyelectrolyte ionic elastomer (Poly(TA-*co*-TAT)-TAO) exhibits remarkable stretchability (> 200%) and elasticity (hysteresis < 7.5%, recovery > 99% at 160% strain). Its long-term creep resistance (creep < 0.4% over 12 hours) makes it an ideal flexible electrode material for applications under sustained high-strain conditions. The flexibility and non-drift in Poly(TA-*co*-TAT)-TAO-based electrodes show promising potential for long-term emotional monitoring. Integrated with wearable EEG acquisition devices, this creep-free polyelectrolyte ionic elastomer not only offers a practical solution to signal drift in polymer-based bio-ionic systems, but also paves the way for reliable, continuous neurophysiological monitoring in daily-life environments.

# Declarations

# Acknowledgments

This work is supported by National Natural Science Foundation of China (22475031), National Youth Top-notch Talent Support Program of China.

# References

1. McIntyre, R. S. *et al.* Bipolar disorders. *The Lancet* **396**, 1841–1856 (2020).
2. Singh, B. *et al.* Bipolar disorder. *The Lancet* **406**, 963–978 (2025).
3. Nierenberg, A. A. *et al.* Diagnosis and Treatment of Bipolar Disorder: A Review. *JAMA* **330**, 1370 (2023).
4. Han, Q. *et al.* Hydrogel Nanoarchitectonics of a Flexible and Self-Adhesive Electrode for Long-Term Wireless Electroencephalogram Recording and High-Accuracy Sustained Attention Evaluation. *Adv. Mater.* **35**, 2209606 (2023).
5. Su, H. *et al.* A Complementary Dual-Mode Ion-Electron Conductive Hydrogel Enables Sustained Conductivity for Prolonged Electroencephalogram Recording. *Adv. Sci.* **11**, 2405273 (2024).
6. Zhao, Z. *et al.* A Thin and Self-Adaptive Artificial Skin Based on Hierarchical Supramolecular Interactions for Multimodal Mental Monitoring. *Adv. Funct. Mater.* e15866 (2025).
7. Kaveh, R. *et al*. Wireless ear EEG to monitor drowsiness. *Nat. Commun.* **15**, 6520 (2024).
8. Xu, Y. *et al.* In-ear integrated sensor array for the continuous monitoring of brain activity and of lactate in sweat. *Nat. Biomed. Eng.* **7**, 1307–1320 (2023).
9. Kim, T. *et al.* Mechanically Robust and Ion-Conductive Polyampholyte Elastomers via Dimeric Ionic Bonding. *Adv. Mater.* e08670 (2025).
10. Sun, T. L. *et al.* Physical hydrogels composed of polyampholytes demonstrate high toughness and viscoelasticity. *Nat. Mater.* **12**, 932–937 (2013).
11. Leocmach, M. *et al*. Creep and Fracture of a Protein Gel under Stress. *Phys. Rev. Lett.* **113**, 038303 (2014).
12. He, Y. *et al*. Creep-free polyelectrolyte elastomer for drift-free iontronic sensing. *Nat. Mater.* **23**, 1107–1114 (2024).
13. Jang, T.-M. *et al.* Stretchable and biodegradable self-healing conductors for multifunctional electronics. *Sci. Adv.* **10**, eadp9818 (2024).
14. Wu, P. *et al.* A Robust Core-Shell Nanofabric with Personal Protection, Health Monitoring and Physical Comfort for Smart Sportswear. *Adv. Mater.* **36**, 2411131 (2024).
15. Wang, Y. *et al*. Adaptive Ionogel Paint from Room-Temperature Autonomous Polymerization of α-Thioctic Acid for Stretchable and Healable Electronics. *Adv. Funct. Mater.* **31**, 2101494 (2021).
16. Yang, D. *et al.* A Rational Design of Bio-Derived Disulfide CANs for Wearable Capacitive Pressure Sensor. *Adv. Mater.* **36**, 2403880 (2024).

17. Liu, Y. *et al.* Highly Strong and Tough Supramolecular Polymer Networks Enabled by Cryptand-Based Host-Guest Recognition. *Angew. Chem. Int. Ed.* **62**, e202302370 (2023).
18. Dewapriya, M. A. N. *et al*. Strain rate effects on the axial tensile behavior of crystalline polyethylene: Insights from molecular dynamics simulations. *Polymer* **295**, 126779 (2024).
19. Kim, H. & Choi, J. Influence of crystalline structure on creep resistance capability in semi-crystalline Polymers: A coarse-grained molecular dynamics study. *Int. J. Fatigue* **188**, 108517 (2024).
20. Sadat, M. R. *et al*. A molecular dynamics study of the role of molecular water on the structure and mechanics of amorphous geopolymer binders. *J. Chem. Phys.* **145**, 134706 (2016).
21. Sahputra, I. H. & Echtermeyer, A. T. Molecular dynamics simulations of strain-controlled fatigue behaviour of amorphous polyethylene. *J. Polym. Res.* **21**, 577 (2014).
22. Schlögl, A. *et al.* A fully automated correction method of EOG artifacts in EEG recordings. *Clin. Neurophysiol.* **118**, 98–104 (2007).
23. Sikander, G. & Anwar, S. Driver Fatigue Detection Systems: A Review. *IEEE Trans. Intell. Transp. Syst.* **20**, 2339–2352 (2019).
24. Xiong, L. *et al*. Sustainable development of electroencephalography materials and technology. *SusMat* **4**, e195 (2024).
25. Zentner, M. *et al*. Emotions evoked by the sound of music: Characterization, classification, and measurement. *Emotion* **8**, 494–521 (2008).
26. Liu, L. *et al.* Dynamic Nanoconfinement Enabled Highly Stretchable and Supratough Polymeric Materials with Desirable Healability and Biocompatibility. *Adv. Mater.* **33**, 2105829 (2021).
27. Jiang, Z. *et al.* A 1.3-micrometre-thick elastic conductor for seamless on-skin and implantable sensors. *Nat. Electron.* **5**, 784–793 (2022).
28. Li, T. *et al*. Healable Ionic Conductors with Extremely Low-Hysteresis and High Mechanical Strength Enabled by Hydrophobic Domain-Locked Reversible Interactions. *Adv. Mater.* **35**, 2307990 (2023).
29. Cui, N. *et al.* Stretchable transparent electrodes for conformable wearable organic photovoltaic devices. *Npj Flex. Electron.* **5**, 31 (2021).

# Methods

Materials

All chemicals were obtained from Aladdin and Adamas, China, and used as received without further purification.

Synthesis of TAT

Thioctic acid (TA, 41.5 g, 0.2014 mol, 1.3 equiv) and 3-bromo-1-propanol (22.2 g, 0.1549 mol, 1.0 equiv) were dissolved in dichloromethane (DCM, 350 mL). To this solution at 0 °C were sequentially added DMAP (2.5 g, 0.0295 mol, 0.19 equiv) and DCC (48.0 g, 0.2326 mol, 1.5 equiv). After stirring for 1 h at

0 °C, the reaction mixture was allowed to warm to room temperature and stirred for 36 h. The crude product was filtered, concentrated under reduced pressure, and purified by column chromatography ($SiO_2$, PE/EA = 4:1) to afford TA-Br as a yellow oil (54.8 g, 86 wt%).

TA-Br (20.0 g), 1-methylimidazole (5.0 g), and 2,6-di-tert-butyl-4-methylphenol (0.2 g) were dissolved in DCM (150 mL) and refluxed at 39°C under $N_2$ for 40 h. After solvent removal, the crude product was washed with ethyl acetate (EA), dissolved in DCM, and concentrated to obtain cationized imidazolyl thioctic acid ($[TA]^+[Br]^-$, TAB) as a yellow oil (18.8 g, 75 wt.%).

A mixture of LiTFSI (7.5 g) in DI water (150 mL) was added to TAB (10.0 g) and stirred at room temperature for 2 h. The product, $[TA]^+[TFSI]^-$ (TAT), was extracted with DCM (250 mL) and the organic layer was washed three times with DI water. After drying over anhydrous $Na_2SO_4$, the solvent was removed under reduced pressure at room temperature to afford TAT (42.3 g, 82 wt%).

Synthesis of TAO

Thioctic acid (TA, 20.0 g, 0.0969 mol, 2.1 eq) and Tetraethyleneglycol (9.0 g, 0.0463 mol, 1.0 eq) were dissolved in dichloromethane (DCM, 200 mL). DMAP (2.2 g, 0.0179 mol, 0.38 eq) and DCC (22.0 g, 0.1065 mol, 2.3 eq) were sequentially added to the solution at 0°C. After 1 h stirring at 0°C, the reaction mixture was warmed to room temperature and stirred for 36 h. The crude product was filtered, concentrated, and purified by column chromatography ($SiO_2$, PE/EA = 4:1) to yield TAO as a yellow oil (16.6 g, 55 wt.%).

Synthesis of Poly(TA-*co*-TAT)

TAT (2 g, 0.0033 mol) and TA (0.6765 g, 0.0033 mol) were dissolved in ethanol (4 mL) and stirred at room temperature for 2 h. The solution was then concentrated under reduced pressure and thermally polymerized at 60 °C under vacuum for 5 h to form Poly(TA-*co*-TAT).

Synthesis of Poly(TA-*co*-TAT)-TAO

TAT (2 g, 0.0033 mol) and TA (0.6765 g, 0.0033 mol) were mixed with TAO, and the mixture was dissolved in ethanol (4 mL) and stirred at room temperature for 2 h. The solution was then concentrated under reduced pressure and thermally polymerized at 60 °C under vacuum for 5 h to form Poly(TA-*co*-TAT)-TAO. The addition amount of TAO is 0.5 mol% (0.0187 g), 1.0 mol% (0.0374 g), 1.5 mol% (0.0562 g), and 2.0 mol% (0.0748 g).

Synthesis of PVDF-HFP/[EMIM][TFSI] ionogel

PVDF-HFP (1.0 g) was dissolved in acetone (10 g) with stirring at room temperature for 1 h. Subsequently, [EMIM][TFSI] (3.0 g for PVDF-1 or 6.0 g for PVDF-2, corresponding to mass ratios of 3:1 and 6:1 relative to PVDF-HFP, respectively) was added, and stirring was continued for another hour. The homogeneous mixture was cast into a polytetrafluoroethylene (PTFE) mold, allowed to stand at room

temperature for 3 h, and then dried at 40 °C for 2 h to evaporate the solvent, yielding the final PVDF-HFP/[EMIM][TFSI] ionogel.

Synthesis of PolyTA/[EMIM][TFSI]

Thioctic acid (TA, 3.0 g) was dissolved in ethanol (6 mL) with stirring at room temperature for 1 h. Subsequently, [EMIM][TFSI] was added (1.0 g for PTA-IL-1 or 0.5 g for PTA-IL-2, corresponding to IL-to-TA mass ratios of 1:3 and 1:6, respectively), and stirring was continued for another hour. The mixture was concentrated under reduced pressure and then subjected to thermal polymerization at 60 °C under vacuum for 5 h to afford the final product, PolyTA/[EMIM][TFSI].

Synthesis of PAM Hydrogel

A photo-initiator 1173 and crosslinker HDDA were mixed with Acrylamide (AM) of 0.5 mol% and 3 mol%, and the mixture was dissolved in DI water (Final solid content: 20%), respectively, with respect to the total amount of monomer, and the mixture was exposed to ultraviolet light (365 nm) for 3 h for the polymerization of PAM hydrogel.

Synthesis of PVA-LiTFSI Elastomer

Poly(vinyl alcohol) (PVA, 5.0 g) was dissolved in N,N-dimethylformamide (DMF, 15 g) with stirring at 40 °C for 1 h. Lithium bis(trifluoromethanesulfonyl)imide (LiTFSI, 2.5 g) was then added to the solution, and stirring was continued at 40 °C for another hour. The mixture was concentrated under reduced pressure, followed by thermal evaporation at 80 °C under vacuum for 24 h to afford the final PVA-LiTFSI elastomer.

Mechanical characterizations of Poly(TA-*co*-TAT)-TAO

All mechanical characterizations were performed using an Instron 5943 universal testing machine with a 10 N load cell unless otherwise specified. For the tensile test, the samples were cut into a rectangular shape, 30 mm in gauge length, 5 mm in width and 0.15 mm in thickness and clamped to the machine. The strain rate was 30 mm $min^{-1}$. For the loading and unloading tests, hysteresis was calculated by dividing the area enclosed by the loading and unloading curves by the area under the loading curve. Rheological experiments were carried out using a TA Instruments ARES G2 stress-controlled rheometer with an 8.0 mm parallel plate attachment. Stress relaxation measurements were carried out under strain amplitude 5% at temperatures from 30 to 80 $^{o}$C for Poly(TA-*co*-TAT)-TAO and from 30 to 70 $^{o}$C for Poly(TA-*co*-TAT), respectively. For the creep test, or the static fatigue test, the sample was stretched stepwise to a stress of 30 kPa and maintained for 12 h or 24 h. Master curves of storage modulus (G') and loss modulus (G") were obtained by time-temperature superposition (TTS) shifts at a reference temperature of 30 $^{o}$C. Based on the Arrhenius plot of the temperature-dependent horizontal shift factors, apparent activation energies ($E_a$) were calculated from the slope of the curve. Two rectangular copper foils (5 × 5 $mm^2$) contacting the two ends of the sample were connected to a resistance meter to

measure the impedance at a frequency of 1 MHz and a test voltage of 0.5 V. During the test, the displacement and impedance of the samples were continuously measured. For the compressive test, the samples were cut into a square with a side length of 10 mm. A thin layer of lubricating oil was applied to the top and bottom surfaces of the sample to minimize the friction between the compression fixture and the sample. For monotonic compression, the loading velocity was 10 mm $min^{-1}$. For the fatigue test, the testing machine was an Instron 5943 universal testing machine with a 1 kN load cell with a force control mode applying triangular waves ranging from 0 to 30 kPa at a frequency of 1 Hz.

Electrical characterizations of Poly(TA-*co*-TAT)-TAO

The ac-impedance spectra were measured using 0.15-mm-thick circular samples of diameter 8 mm, using the electrochemical workstation Autolab PGSTAT302N at an amplitude of 100 mV and within the frequency range of 5 Hz to 1 MHz. Before the test, the sample is clamped between two copper plates (10 μm). The data were fitted to the equivalent circuit model and the results of Poly(TA-*co*-TAT)-TAO and Poly(TA-*co*-TAT) are shown in Supplementary Fig. 35. Electrical measurements utilized a Semight S3012H source meter coupled to an EPSA200 translation stage with OLCU-2-SS motion controller. Relative resistance change ($\Delta R/R_0$) was calculated according to equations (1):

$$\Delta R/R_0=(R-R_0)/R_0 \quad (1)$$

where $R_0$ is the resistance without strain applied, R is the resistance with strain applied, and ΔP is the tensile change.

Emotion-related EEG signal acquisition test

This study involved data collection to investigate the relationship between emotional states and ear-EEG signals. Five participants (three male and two female), aged between 22 and 26, were recruited for emotion-induction and EEG recording. The experiment was conducted in a quiet environment maintained at 25 $^{o}$C. Using internationally validated emotional stimuli, we recorded the subjects' EEG signals and annotated the data with emotional categories (namely happiness, sadness, fear, disgust, surprise, anger, and calmness) along with corresponding timestamps.

Structural characterizations and measurements

The nuclear magnetic resonance (NMR) spectra were acquired using Brüker AV-400 ($^{1}$H NMR, 400 MHz), AV-600 ($^{13}$C NMR, 150 MHz), and AV-600 ($^{19}$F-NMR, 376 MHz) spectrometers with $CDCl_3$ as both solvent and internal standard. Electrospray ionization mass spectrometry (ESI-MS) analysis was conducted on a Shimadzu LCMS-IT-TOF mass spectrometer. The SEM images were taken using a field-emission scanning electron microscope (ZEISS Sigma 360). These cell fluorescence images were captured using a laser confocal scanning microscope (Leica TCS SPE Confocal Microscope). X-ray diffraction (XRD) patterns were collected on a Rigaku Ultima IV powder diffractometer equipped with a rotating Cu Kα anode (λ = 1.5418 Å, 18 kW, 450 mA), automated curved graphite monochromator, and programmable

variable slit system. The Raman spectra were acquired using a Renishaw inVia micro-Raman spectrometer with 785 nm excitation, coupled to a Leica DMLM microscope. ATR-FTIR spectra were taken on a Nicolet iS50 (Thermo Fisher Scientific) spectrometer with a diamond ATR crystal as the window material. Temperature-variable FTIR spectra of the ionogel were collected in the transmission mode, and the sample was sealed in two KBr tablets for heating. Gel permeation chromatography (GPC) analysis of Poly(TA-*co*-TAT) was conducted using a Waters 1525 system equipped with a Waters 2414 detector and Agilent Plgel 5 μm MIXED-C column, with DMF as the mobile phase. Atomic force microscopy (AFM) imaging was performed on a Bruker Dimension Icon Bio microscope. The hydrophilic and hydrophobic properties are tested on a fully automatic contact angle instrument (dataphysics OCA-50AF). Thermal characterization employed a TA Q2000 differential scanning calorimeter at a heating rate of 10°C $min^{-1}$. The transition points of elastomer were measured on DSC (TA Q250) with a heating rate of 10 $^{o}C\ min^{-1}$ under nitrogen flow. The stretched samples were transferred into an EPR 5 mm glass capillary, and the capillary was sealed after being degassed. EPR measurements were carried out on a JEOL JES-X320 X-band EPR spectrometer equipped. The spectra of stretched samples were measured using a microwave power of 0.998 mW and field modulation of 0.4 mT with a time constant of 0.03 s and a sweep rate of 1.5 mT/s at r.t. The microwave frequency during the test was 9.807 GHz. The g value was calculated according to the following equation:

$$g = \frac{hv}{\beta H} \quad (2)$$

where *h* is the Planck constant, *v* is the microwave frequency, $\beta$ is the Bohr magneton, and *H* is the magnetic field.

In situ WAXS and SAXS analyses were measured using a Xeuss 3.0 SAXS/WAXS system (Xenocs SA, France). A Cu K$\alpha$ X-ray source (GeniX3D Cu ULD), operating at 50 kV and 0.6 mA, produced radiation with a wavelength of 1.5418 Å. An Eiger 2R Hybrid pixel photon counting detector (500K model, vacuum compatible, windowless) with a silicon sensor at a thickness of 450 μm and a resolution of 512 × 1028 pixels (pixel size = 172 × 172 $\mu m^2$) was used to collect the scattered signals. Each SAXS pattern was collected after a 5 min exposure. 1D intensity profiles were integrated from background-corrected 2D SAXS patterns. Crystal sizes were calculated using the Scherrer equation:

$$D = \frac{K\lambda}{\beta cos\theta} \quad (3)$$

where *D* is the average size of the crystal domains and *K* is dimensionless shape factor of ≈0.89, $\beta$ is the line broadening at half the maximum intensity (FWHM) after subtracting the instrumental line broadening, $\theta$ is the Bragg angle. The long-period was calculated by Bragg's law:

$$L = \frac{2\pi}{q} \quad (4)$$

where *L* represents the long-period and *q* is the scattering vector. Strains marked in figures refer to positions of fixtures in the tensile equipment.

# Figures

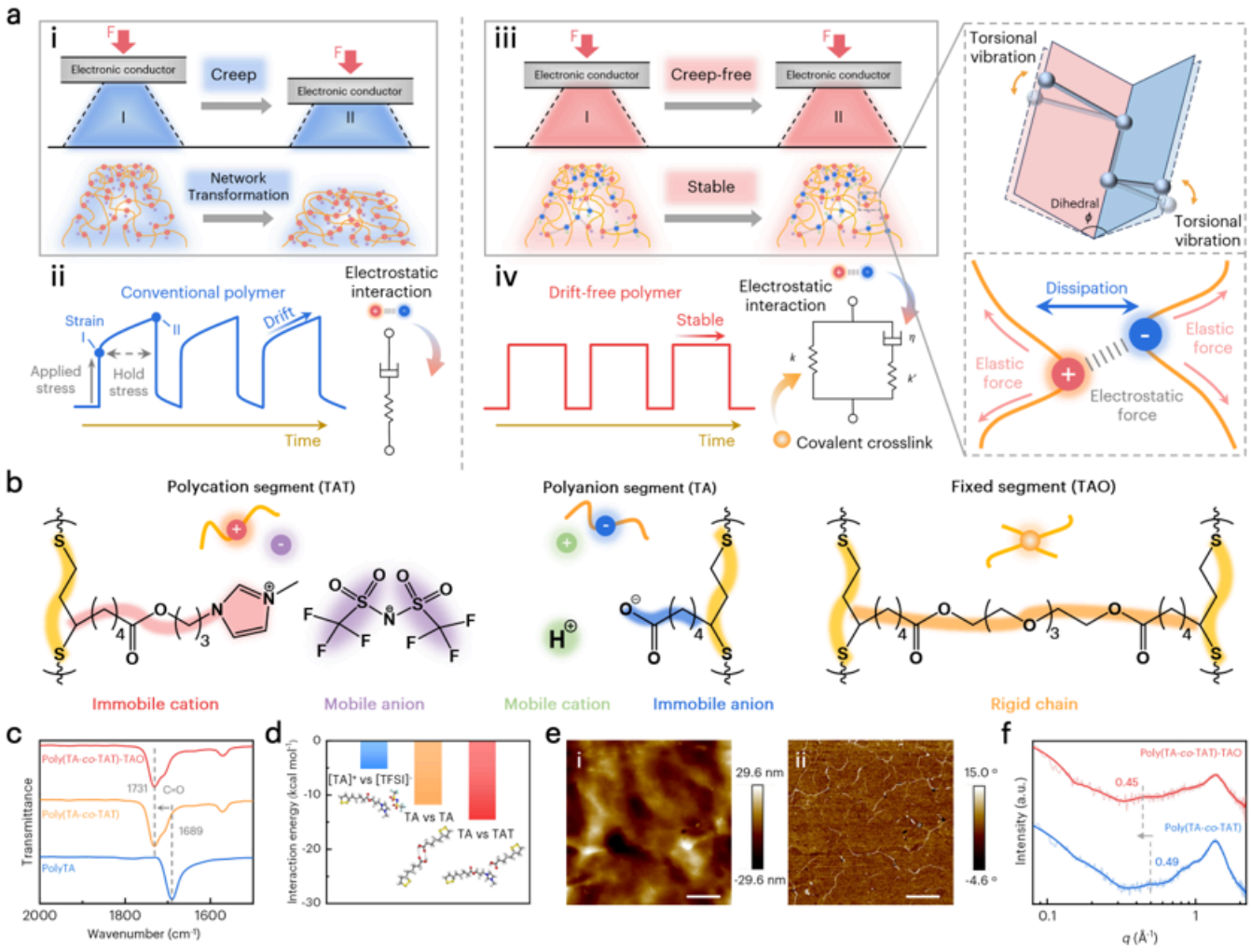
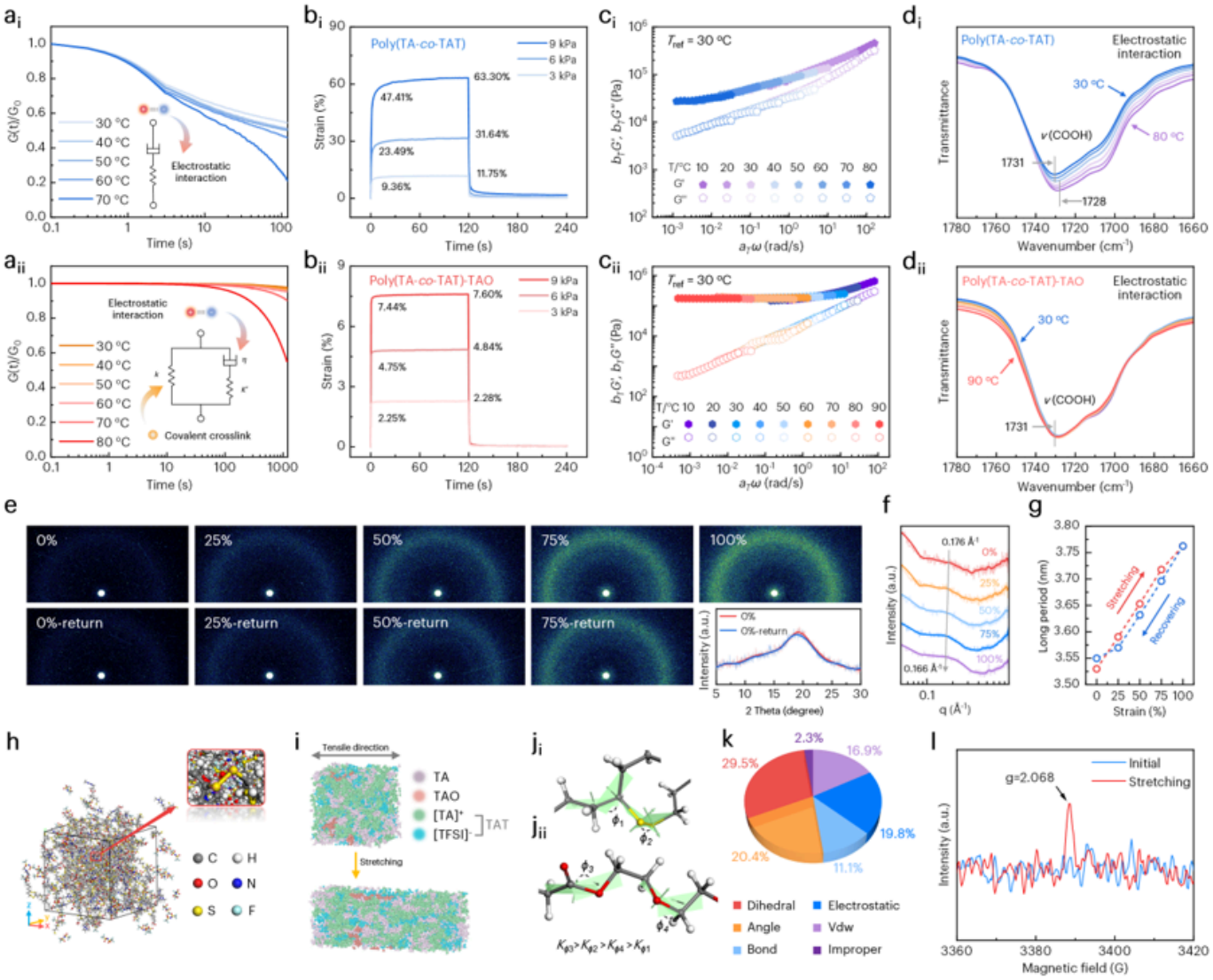



**Figure 1**

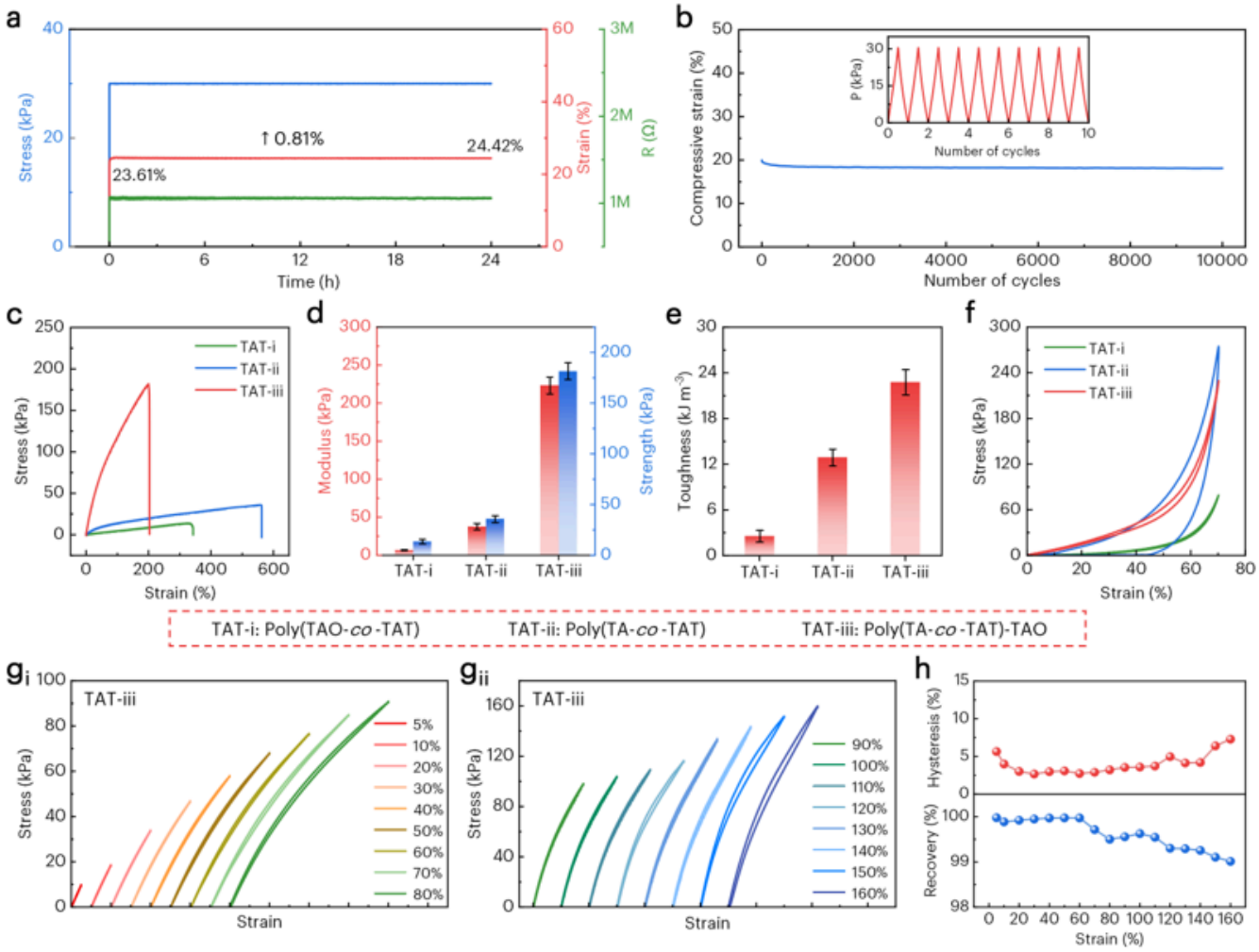
**Design principles and characterization. a**, Designing principles of a creep-free polyelectrolyte elastomer for non-drift electrical signal acquisition. 'F' represents the applied force. **b**, The monomer structure of the creep-free polyelectrolyte network. **c**, Local ATR-FTIR spectra of PolyTA, Poly(TA-*co*-TAT), and Poly(TA-*co*-TAT)-TAO. **d**, Calculated interaction energies in three pairs of components by molecular dynamics simulation. **e**, AFM (i) height and (ii) phase maps of Poly(TA-*co*-TAT)-TAO. Scale bar = 1 μm. **f**, Wide-angle x-ray scattering (WAXS) spectra of Poly(TA-*co*-TAT) and Poly(TA-*co*-TAT)-TAO. *L* represents the scattering vector between backbones, with a corresponding correlation distance *L* given by the relation $L = 2\pi / q$.




## Figure 2

**Creep-free behavior analysis and its mechanism. a**, Stress relaxation tests of (**a$_i$**) Poly(TA-*co*-TAT) and (**a$_{ii}$**) Poly(TA-*co*-TAT)-TAO at different temperatures. **b**, Creep-recovery curves of (**b$_i$**) Poly(TA-*co*-TAT) and (**b$_{ii}$**) Poly(TA-*co*-TAT)-TAO with different stress levels. **c**, Master curves of (**c$_i$**) Poly(TA-*co*-TAT) and (**c$_{ii}$**) Poly(TA-*co*-TAT)-TAO at a reference temperature of 30 $^{o}$C. **d**, Temperature-variable FTIR spectra of (**d$_i$**) Poly(TA-*co*-TAT) in the C=O stretching region from 30 to 80 $^{o}$C (interval: 10 $^{o}$C), and (**d$_{ii}$**) Poly(TA-*co*-TAT)-TAO in the C=O stretching region from 30 to 90 $^{o}$C (interval: 10 $^{o}$C). **e**, The selected 2D WAXS and 1D WAXS patterns of Poly(TA-*co*-TAT)-TAO performed at different strains including both the stretching and the recovery process. **f**, The selected 1D SAXS patterns of Poly(TA-*co*-TAT)-TAO performed during the tensile process under different strains. **g**, Evolution of long-period strain dependence of Poly(TA-*co*-TAT)-TAO. **h**, Schematic diagram of Poly(TA-*co*-TAT)-TAO model (the enlarged partial view shows the disulfide bond undergoing reaction). **i**, Molecular dynamics simulations reveal the relative movements between TAO and polymer chains during the stretching process. **j**, Dihedral structure. The dihedral coefficients of

($\mathbf{j_i}$) carbon-sulfur backbone ($K_{\phi 1}$ and $K_{\phi 2}$) and ($\mathbf{j_{ii}}$) TAO ester-based backbone ($K_{\phi 3}$ and $K_{\phi 4}$). **k**, The proportion of potential energy components in Poly(TA-*co*-TAT)-TAO. **l**, EPR spectra of Poly(TA-*co*-TAT)-TAO indicating the presence of sulfur radical.




## Figure 3

**Mechanical properties. a**, The variations of strain and impedance of Poly(TA-*co*-TAT)-TAO with time under a constant tensile stress of 30 kPa. **b**, The variation of the peak strain of Poly(TA-*co*-TAT)-TAO with time under cyclic tension with a maximum stress of 30 kPa. The inset shows the loading profile. **c**, Uniaxial tensile stress-strain curves of Poly(TAO-*co*-TAT), Poly(TA-*co*-TAT), and Poly(TA-*co*-TAT)-TAO. **d-f**, Modulus and strength (**d**), toughness (**e**) and uniaxial compressive stress-strain (**f**) curves of these three materials. $\mathbf{g_{i\text{-}ii}}$, Cyclic stress-strain curves of Poly(TA-*co*-TAT)-TAO with different strains: ($\mathbf{g_i}$) 5-80%, ($\mathbf{g_{ii}}$) 90-160%. **h**, Hysteresis and recovery as a function of strain.

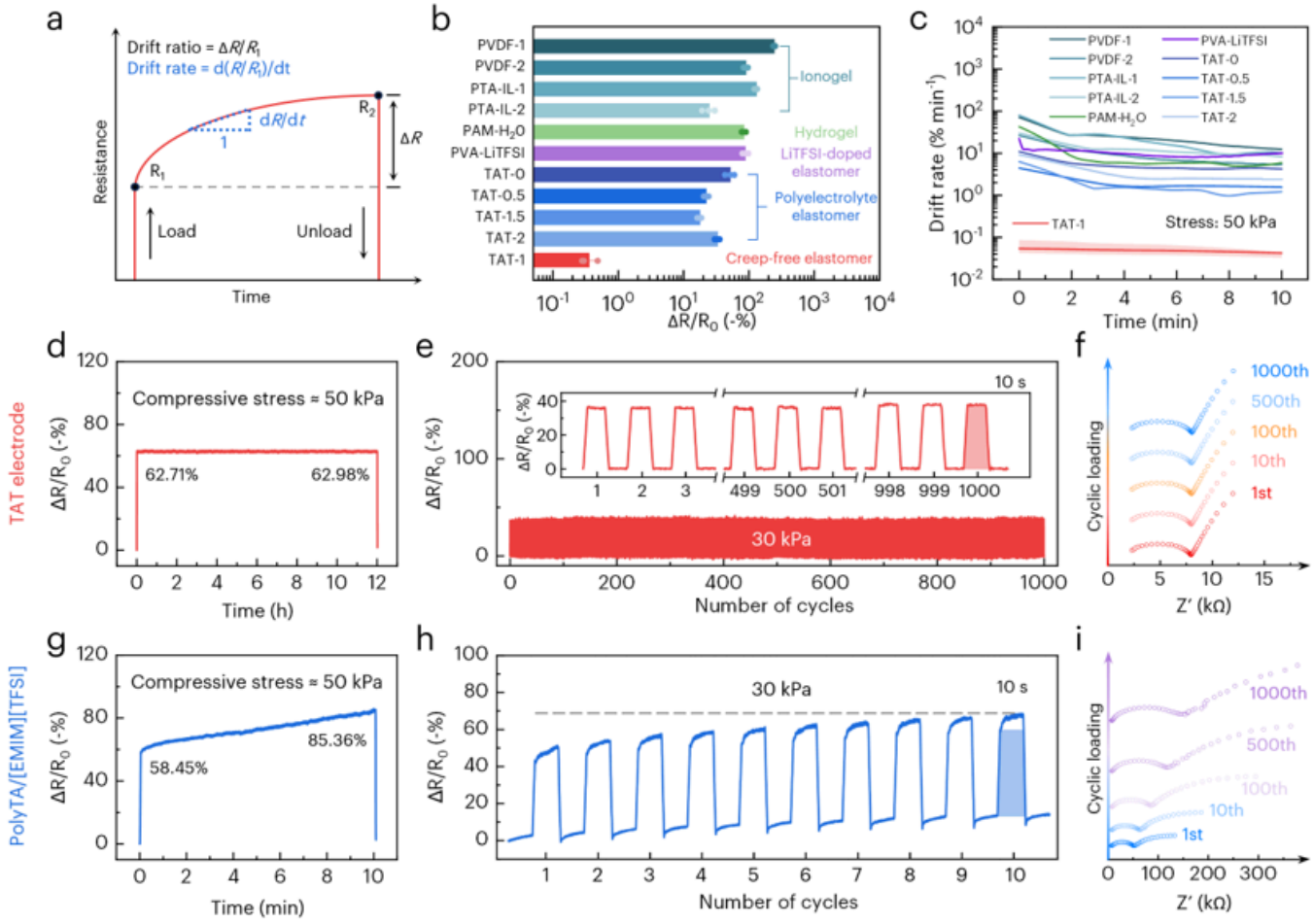
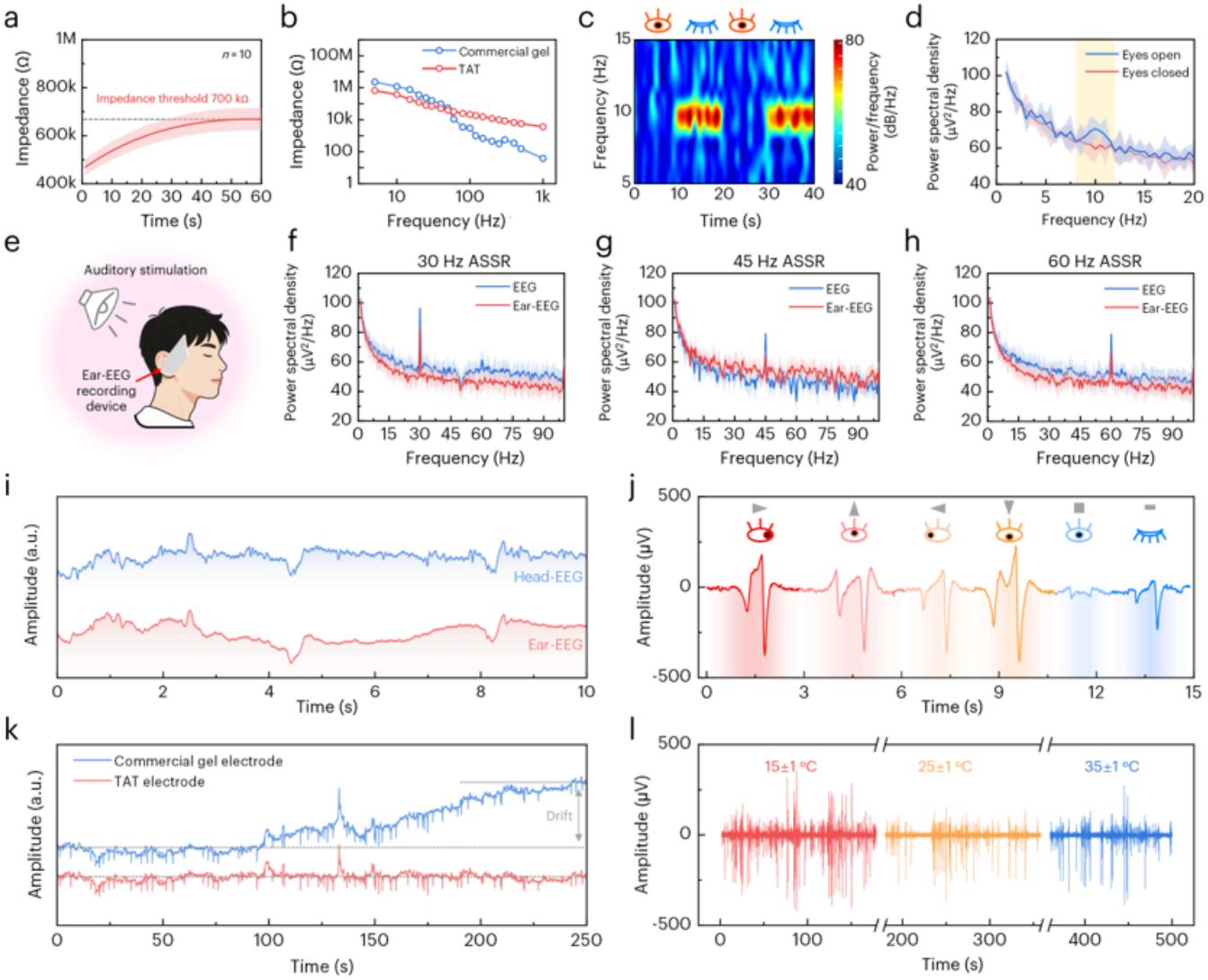



**Figure 4**

**Electrical properties. a**, Definition of drift ratio and drift rate. **b**, Comparison of the drift ratios of polymer electrode based on different ionic conductors under the same pressure (~50 kPa) for 10 min. TAT-1 represents TAT with a crosslink density of 1%. **c**, The variations of drift rate with time for different polymer electrode under a pressure of ~50 kPa. **d**, $\triangle R/R_0$ of the TAT electrode varies with time under static compression of 50 kPa for 12 h. **e**, Cyclic compression of the TAT electrode under square waves, each endures for 10 s, over 1,000 cycles at 30 kPa. The inset zooms in on the signals at the initial, middle and final three cycles. **f**, Electrochemical impedance spectroscopy (EIS) plots of the TAT electrode after cyclic compression ($1^{st}$, $10^{th}$, $100^{th}$, $500^{th}$, and $1000^{th}$). **g**, $\triangle R/R_0$ of the PolyTA/[EMIM][TFSI] electrode varies with time under static compression of 50 kPa for 10 min. **h**, Cyclic compression of the PolyTA/[EMIM][TFSI] electrode under square waves, each endures for 10 s, over 10 cycles at 30 kPa. **i**, EIS plots of the PolyTA/[EMIM][TFSI] electrode after cyclic compression ($1^{st}$, $10^{th}$, $100^{th}$, $500^{th}$, and $1000^{th}$).




## Figure 5

**TAT electrode for electroencephalogram monitoring. a-b**, Electrode-ear impedance characterization with (**a**) impedance magnitude over time upon insertion, and (**b**) impedance magnitude in steady state after insertion for more than 1 min. **c-d**, EEG characterization with (**c**) spectrogram and (**d**) power spectrum density (PSD) for alpha modulation experiments with participants opening and closing their eyes at 10-s intervals. The yellow-shaded interval denotes the 8-12 Hz alpha band in the EEG spectrum. **e-h**, Auditory steady-state test. (**e**) Schematic diagram of auditory steady-state test. Auditory steady state response (ASSR) PSDs for three acoustic stimuli amplitude modulated at (**f**) 30 Hz, (**g**) 45 Hz, and (**h**) 60 Hz.Signal-to-Noise Ratio of the 30 Hz, 45 Hz, and 60 Hz were 10.7 ± 1.1 dB, 10.1 ± 1.2 dB, and 11.2 ± 1.8 dB, respectively. **i**, Comparison of signals collected by Source-EEG and ear-EEG. **j**, Transient response to various eye movements recorded. **k**, Comparison of long-term stability between TAT electrodes and commercial gel electrodes. **l**, Ear-EEG signals under varying ambient temperatures.

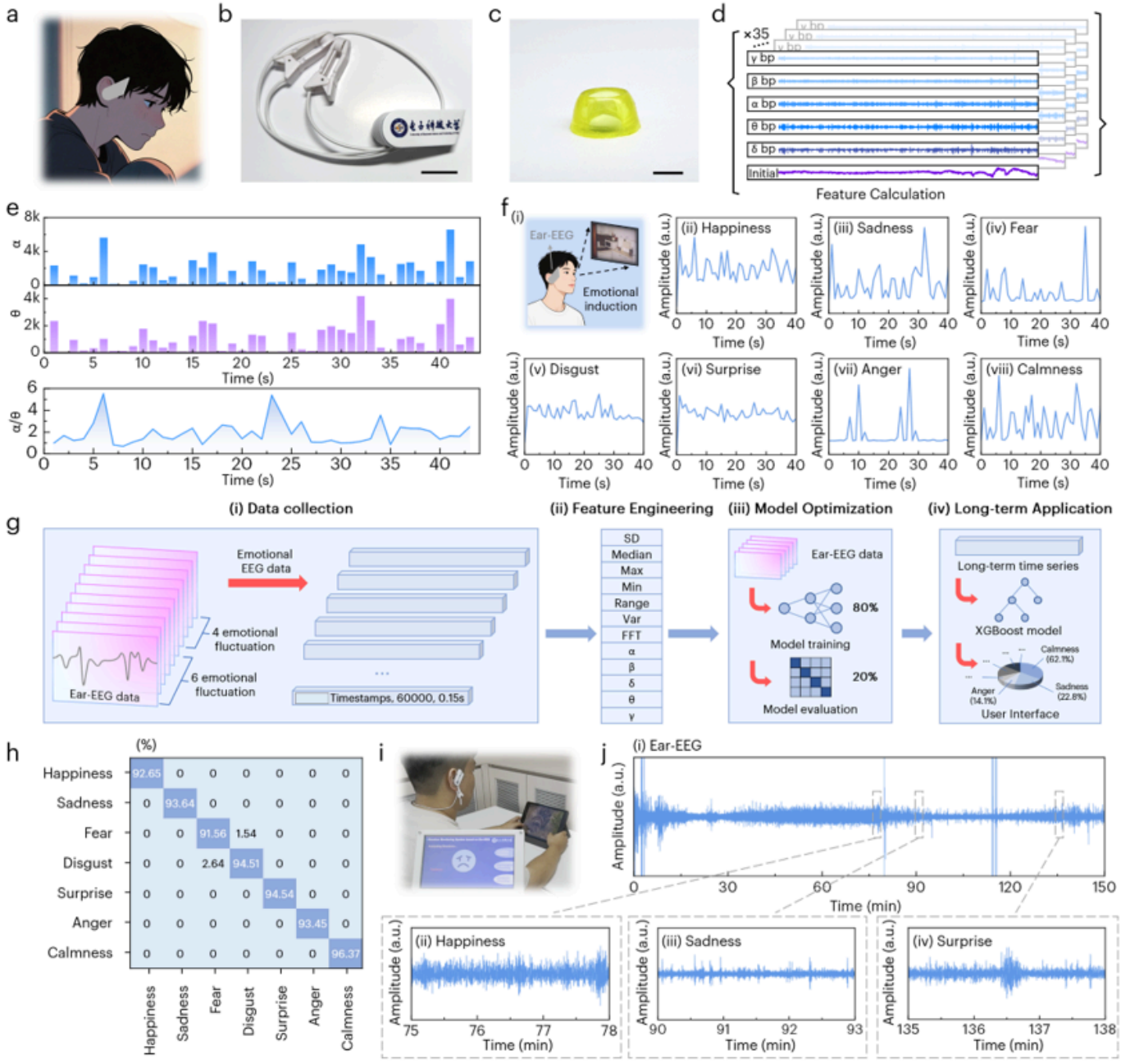



**Figure 6**

**Emotion detection and automatic intervention based on ear-EEG. a,** Application scenario of TAT electrode: bipolar affective disorder. **b,** Wearable ear-EEG acquisition device. Scale bar = 2 cm. **c,** TAT electrode. Scale bar = 1 cm. **d,** Recorded EEG were used to generate features and labels for a brain-state classifier. **e,** Meditation EEG alpha waveband, beta waveband, and meditation state parameters. **f,** ($f_i$) Emotional induction and ($f_{ii}$-$f_{viii}$) ear-EEG signals collected through emotional induction. **g,** Machine learning. **h,** Accuracy of emotion recognition. **i,** Visual output of wearer's emotions. **j,** Long-term ear-EEG signals acquisition.

# Supplementary Files

This is a list of supplementary files associated with this preprint. Click to download.

- SupplementaryVideo1PolyTAcoTAT.mp4
- SupplementaryVideo2PolyTAcoTATTAO.mp4
- SupplementaryVideo3PolyTAcoTATTAO.mp4
- SupplementaryVideo4PolyTAcoTATTAO.mp4
- SupportingInformationCreepfreeionicelastomerfornondriftingearEEGsignalacquisition.docx